Materials Chemistry and Physics 363 (2026) 132800

Contents lists available at ScienceDirect

Materials Chemistry and Physics

journal homepage: www.elsevier.com/locate/matchemphys

Structure and UV emission characteristics of Gd^{3+}-activated $X_2P_2O_7$ (X = Ca, Sr, Ba) pyrophosphates

Didzis Salnajs [a,*], Dace Nilova [a], Jonas Stadulis [b], Anatolijs Sarakovskis [a], Aleksej Zarkov [b], Andris Antuzevics [a]

[a] Institute of Solid State Physics, University of Latvia, Kengaraga 8, LV-1063, Riga, Latvia
[b] Institute of Chemistry, Vilnius University, Naugarduko 24, LT-03225, Vilnius, Lithuania

HIGHLIGHTS

- Host composition influences Gd^{3+} incorporation and persistent luminescence
- Assessed pyrophosphate host bandgaps are suitable for UV-B emission
- EPR identifies oxygen-hole and phosphorus-related radicals after X-ray irradiation
- $Sr_2P_2O_7$: Gd^{3+} exhibits highest-radiance persistent luminescence
- Defect engineering is important for rational design of UV-B phosphors

ARTICLE INFO

Keywords:
Afterglow
Long-lasting luminescence
Thermoluminescence
Electron spin resonance (ESR)
Radiation-induced radicals

ABSTRACT

Ultraviolet-emitting phosphors deliver higher-energy photons than visible or infrared sources, which is a prerequisite for efficient photoionisation and energy transfer processes. In this work, gadolinium-activated alkaline-earth pyrophosphates ($X_2P_2O_7$, X = Ca, Sr, Ba) are comparatively investigated to determine how host composition and structure influence Gd^{3+} incorporation, irradiation-induced defect formation, and UV-B persistent luminescence characteristics. Reflection electron energy-loss spectroscopy (REELS) indicates that all compounds possess suitable bandgap values for UV emission. X-ray diffraction (XRD) and electron paramagnetic resonance (EPR) analyses confirm successful incorporation of Gd^{3+} ions at low-to-moderate doping concentrations into the $X_2P_2O_7$ hosts. All materials exhibit the characteristic Gd^{3+} $^6P_{7/2} \rightarrow {}^8S_{7/2}$ UV-B photoluminescence emission at 312 nm, which is also observed in thermally stimulated luminescence (TSL) measurements following X-ray excitation, with each host showing distinct glow peak temperatures. Spin-Hamiltonian parameters derived from EPR spectra simulations reveal that X-ray irradiation induces the formation of oxygen-related hole centres and phosphorus-related radicals. Among the studied compounds, $Sr_2P_2O_7$: Gd^{3+} exhibits optimal trap depths for intense UV-B persistent luminescence, maintaining radiance above $5 \cdot 10^{-4}$ mW m^{-2} sr^{-1} for nearly 2 h after excitation. These results establish Gd^{3+}-doped pyrophosphates as efficient UV-B phosphors with tuneable defect structures suitable for phototherapy, sterilisation, and photocatalytic applications.

1. Introduction

The importance of phosphors capable of emitting in the ultraviolet (UV) spectral region arises from their higher photon energy compared to those of the visible spectrum. The UV range is conventionally divided into UV-C (200-280 nm), UV-B (280-315 nm), and UV-A (315-400 nm) regions. This high-energy radiation enables a variety of applications that rely on photoionisation or energy transfer processes, including phototherapy [1,2], sterilisation [3], and the possibility of extending the functional operational time of commercial photocatalysts [4–8]. Due to chemical stability and sufficiently large bandgap values, various phosphate-based materials are widely used as matrices for optically active dopants [9–11].

Pyrophosphates, specifically calcium pyrophosphates ($Ca_2P_2O_7$, CPPs), are especially interesting as an alternative to calcium orthophosphates, which are widely used in biomedicine [10]. Doping with

* Corresponding author.
E-mail address: didzis.salnajs@cfi.lu.lv (D. Salnajs).

https://doi.org/10.1016/j.matchemphys.2026.132800
Received 14 November 2025; Received in revised form 22 May 2026; Accepted 12 June 2026
Available online 15 June 2026

near-infrared emitters enables multimodal medical and imaging applications [12], while introducing higher energy UV-emitting centres offers potential for cancer cell inactivation in radiation therapy [13]. CPPs crystallise in three different polymorphs (γ-, β-, and α-), each with distinct Ca coordination, P-O-P angles, P-O bond lengths, and radiation-induced point defect formation. These structural variations influence the local environment of dopant ions and are essential to investigate for the development of both conventional and persistent phosphors [14]. The UV photoluminescence properties of Pr^{3+}-activated α- and β-CPP phases have been described by *Pier* et al., who demonstrated successful dopant incorporation in the lattice and relevance of the materials for bacterial inactivation [11]. *Griesiute* et al. reported phase-dependent visible emission in Mn-activated CPP polymorphs [10], further highlighting the role of crystal structure in optical properties.

Strontium and barium pyrophosphates ($Sr_2P_2O_7$, SPPs; $Ba_2P_2O_7$, BPPs) have also been reported to effectively incorporate a wide range of optically active ions and serve as efficient luminescent materials [15,16], dosimeters [17], and persistent phosphors [18]. Several studies have examined the UV emission characteristics of rare-earth ion-doped SPP. X-ray excitation of Pr^{3+}-doped SPP enables a mechanoluminescent response in the UV-C range, with emission maximum peaking at an exceptionally short wavelength of 230 nm [17]. Gd-activated SPP exhibits intense UV-B persistent luminescence, maintaining a power density of 5.4 mW/m^2 even 60 s after X-ray excitation [18]. Similar to CPPs, SPP and BPP materials crystallise in multiple phases with differing alkaline earth coordinations. Consequently, a systematic comparative investigation of these compounds is essential to determine the structure-property relationships that govern their luminescent behaviour and to guide the design of optimised phosphor materials.

Gd^{3+}-activated hosts effectively emit a narrow crystal-field insensitive UV-B line at 312 nm assigned to the electronic $^6P_{7/2} \rightarrow {}^8S_{7/2}$ 4f-4f transition. Because the 4f levels are well shielded and only weakly perturbed by the lattice [19], the emission wavelength is effectively host-independent, allowing for the optimisation of charge-storage and energy transfer pathways without shifting the emission wavelength. Given the widespread use of the UV-B region in phototherapy, the development of Gd^{3+}-doped persistent phosphors holds significant practical relevance.

Although Gd^{3+}-activated pyrophosphate phosphors have been previously reported, earlier studies have primarily focused on the luminescence performance of individual host materials, while a systematic understanding of how the host composition influences Gd^{3+} incorporation, defect formation and persistent luminescence remains limited. In particular, the relationship between alkaline-earth pyrophosphate hosts, irradiation-induced defect centres and persistent luminescence is still not well understood. Therefore, this work presents a systematic investigation of the structural, optical, and defect-related properties of Gd-activated $X_2P_2O_7$ (X = Ca, Sr, Ba) pyrophosphate materials. By comparing these chemically related hosts, we elucidate how cation size and crystal structure influence dopant incorporation, trap formation, and UV-B emission characteristics. In addition, EPR spectroscopy is employed to identify irradiation-induced defect centres and evaluate their possible role in charge trapping, providing further insight into the persistent luminescence mechanism of Gd^{3+}-activated pyrophosphates. These findings contribute to a more rational understanding of host-dependent persistent luminescence and may support the design of pyrophosphate-based phosphors.

2. Materials and methods

2.1. Material synthesis

CPP polymorphs were synthesised by the wet co-precipitation method [10]. Briefly, a stoichiometric quantity of $Ca(NO_3)_2 \bullet 4H_2O$ (Carl Roth, >99 %) and $Gd(NO_3)_3 \bullet 6H_2O$ (Thermo Scientific, 99.9 %) was dissolved in deionised water to obtain a 0.4 M concentration of metal ions. The desired mol% of Gd^{3+} ions was set according to the target activator concentration relative to Ca^{2+} ions. $(NH_4)_2HPO_4$ (Carl Roth, >98 %) solution of the same concentration was prepared separately and rapidly added to the solution containing metal ions. The mixture was stirred continuously until a white precipitate formed, after which it was aged for 10 min. The precipitate was vacuum-filtered, washed with deionised water, and dried at 90 °C in air. Samples were then annealed at 1000 °C for 5 h to form β-$Ca_2P_2O_7$ and at 1200 °C for 5 h to form α-$Ca_2P_2O_7$. In the case of $Ba_2P_2O_7$ and $Sr_2P_2O_7$, $Ba(NO_3)_2$ (Thermo Scientific, 99 %) and $Sr(NO_3)_2$ (Thermo Scientific, 99 %) were used, and the precipitates for both were annealed at 1000 °C for 5 h. Heating rate for annealing was 5 °C min^{-1}.

2.2. Structural characterisation

The phase composition analysis of the powders was conducted using a Rigaku Miniflex II X-ray diffractometer equipped with a Cu Kα (0.154 nm) radiation source operating at 40 kV and 15 mA. The data were collected within a 10-60° 2θ angle range with a speed of 5° min^{-1}. EPR spectra were recorded with a Bruker ELEXSYS-II E500 spectrometer. Room-temperature measurements were carried out at both X-band (9.836 GHz) and Q-band (34.01 GHz) microwave frequencies. For low-temperature measurements (80 K), the spectrometer was equipped with an Oxford Instruments liquid helium flow cryostat, and spectra were recorded at 9.363 GHz. The microwave power and magnetic field modulation amplitude were optimised individually for each measurement series. Radiation-induced radicals were generated by exposing the samples to X-rays from a tube operated at 45 kV and 10 mA at room temperature for 30 min. Under these conditions, the absorbed dose was

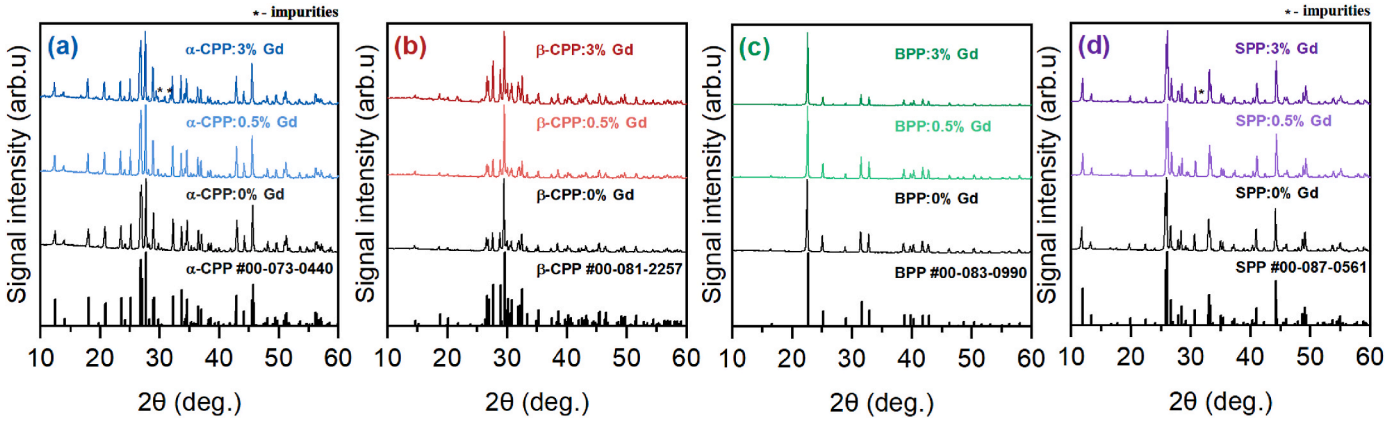

Fig. 1. X-ray diffraction patterns of **(a)** α-CPP, **(b)** β-CPP, **(c)** BPP, and **(d)** SPP samples.

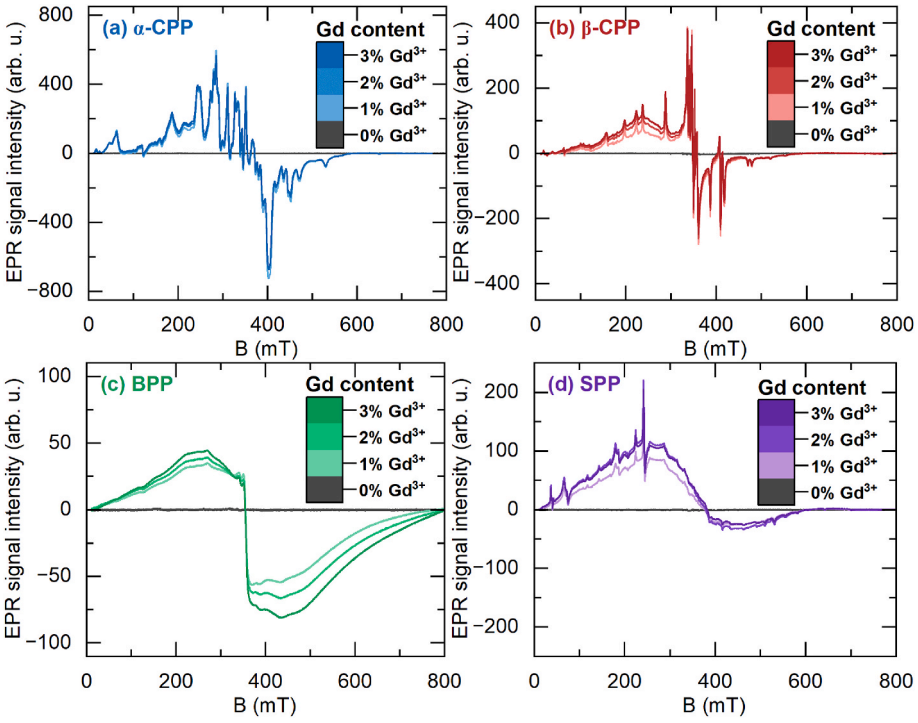

Fig. 2. X-band EPR spectra (10 mW microwave power; 0.4 mT magnetic field modulation amplitude) of **(a)** α-CPP, **(b)** β-CPP, **(c)** BPP, and **(d)** SPP samples. EPR signal intensities are normalised to 100 mg of sample mass.

estimated to be approximately 1 kGy. Following irradiation, the samples were subjected to isochronal annealing in air using a custom-built furnace, with each annealing step maintained for 10 min. EPR spectra simulations were performed using the EasySpin software [20]. The bandgap of the investigated pyrophosphates was evaluated by reflected electron energy loss spectroscopy (REELS) measured by Thermo Fisher Scientific ESCALAB Xi+; electron energy was 1000 eV, with the detector pass energy of 10 eV and measurement step size of 0.02 eV. The binding energy scale was calibrated using sputter-cleaned Au, Ag, and Cu reference samples, setting the Au $4f_{7/2}$, Ag $3d_{5/2}$, and Cu $2p_{3/2}$ peaks at 83.9, 368.2, and 932.6 eV, respectively.

2.3. Optical characterisation

Photoluminescence excitation and emission measurements were carried out at room temperature using an Edinburgh Instruments FLS1000 photoluminescence spectrometer equipped with a gas discharge Xe lamp (CW 450W) used for excitation and a PMT R928P for signal acquisition. The measured powders were pressed in stainless-steel cup sample holders. The positioning of the samples and the operating current of the excitation source were kept equal for all measurements. Thermally stimulated luminescence (TSL) was measured using a Lexsyg research TSL/OSL reader from Freiberg Instruments. Emission spectra were recorded with an Andor DV420A-BU2 CCD camera coupled to the TSL reader (integration time 2 s). Persistent luminescence optical emission power was detected using a UV-extended Si standard photodiode sensor S120VC/PM100D console from Thorlabs. Samples were mechanically rotated in and out of X-ray excitation using a custom turntable system, as described previously [21]. The samples were irradiated with a tungsten-anode X-ray tube operated at 40 kV and 0.5 mA.

3. Results

3.1. Structural characterization

Fig. 1 shows X-ray diffraction patterns for the investigated pyrophosphate polymorphs. Overall, good agreement with the reference data is observed; however, upon increasing the Gd concentration, α-CPP and SPP diffraction patterns exhibit additional signals not attributable to the reference card. The additional peaks can be matched to the $GdPO_4$ (#00-032-0386) impurity phase, indicating a limited solubility of Gd^{3+} in α-CPP and SPP at higher concentrations. In addition, evaporation of phosphate species during high-temperature annealing cannot be excluded and may contribute to secondary phase formation [22]. Phase transition temperatures for the three known CPP polymorphs are as follows: 750 °C for the transition of γ-CPP to β-CPP and 1170 °C for the high temperature transition from β-CPP to α-CPP [23]. α-CPP crystallises in the monoclinic space group $P2_1/n$ (#14) and contains two distinct Ca sites, both being 8-coordinate [CaO_8] dodecahedra. In contrast, β-CPP adopts the tetragonal space group $P4_1$ (#76) with 4 distinct Ca incorporation sites - Ca1 and Ca3 are 7-coordinate (distorted pentagonal bipyramids), Ca4 is 8-coordinate (bicapped trigonal prism), and Ca2 is 9-coordinate (tricapped trigonal prism) [11,24]. The high-temperature forms of α-$Sr_2P_2O_7$ (SPP) and σ-$Ba_2P_2O_7$ (BPP) crystallise in orthorhombic *Pnma* (#62) and hexagonal *P62 m* (#189) space groups, respectively [25,26]. SPP contains two non-equivalent Sr^{2+} sites, both 9-coordinate [SrO_9] [18,25], while Ba^{2+} in BPP occupies 2 unique sites, of which one is 7-coordinate and the other is 10-coordinate [10,11]. Due to the large differences in effective ionic radii of Gd^{3+} (0.94 Å, CN = 6, to 1.11 Å, CN = 9) [27] and P^{5+} (0.17 Å, CN = 4) [28], it is reasonable to assume the incorporation of Gd^{3+} in Ca^{2+}, Ba^{2+}, or Sr^{2+} sites of the pyrophosphate lattice. Such substitution requires charge compensation, which may occur through the formation of intrinsic defects, most plausibly alkaline earth cation vacancies [29].

EPR spectra of the pyrophosphate samples in Fig. 2 reveal concentration-dependent incorporation of Gd^{3+} ions into the materials. The EPR spectra exhibit complex resonance patterns covering a broad magnetic field range. The resonance positions are unique to each matrix, which implies different crystal field environments for the rare-earth ion. Two types of features can be distinguished in the EPR spectra: (1) narrow resonance lines with comparable intensities for all samples, which originate from isolated Gd^{3+} centres, substituting the X^{2+} (X = Ca, Sr,

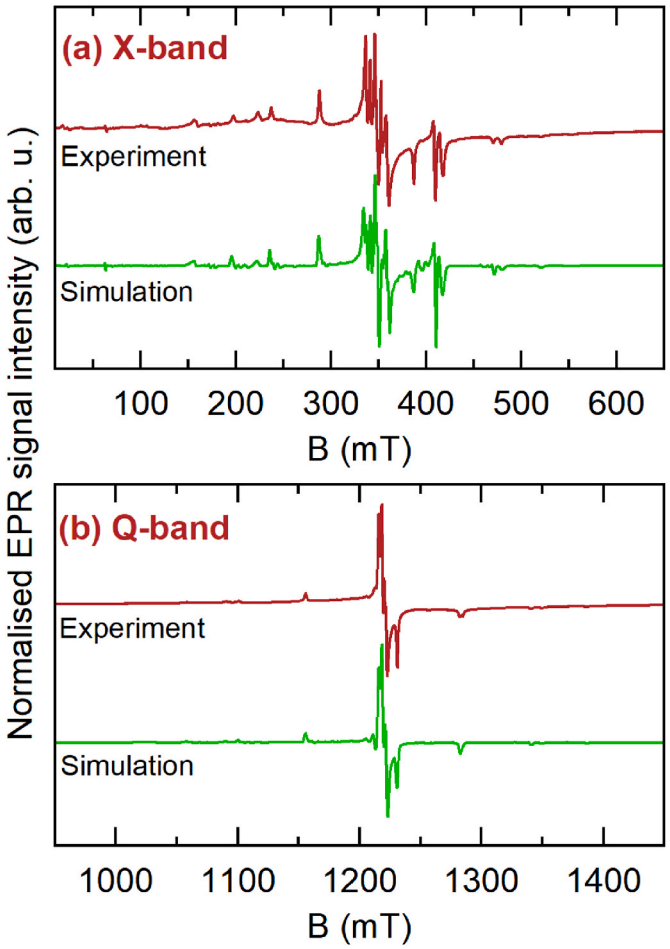

Fig. 3. **(a)** X-band and **(b)** Q-band EPR spectra (10 mW; 0.4 mT) simulations of the β-CPP: 0.5 % Gd sample.

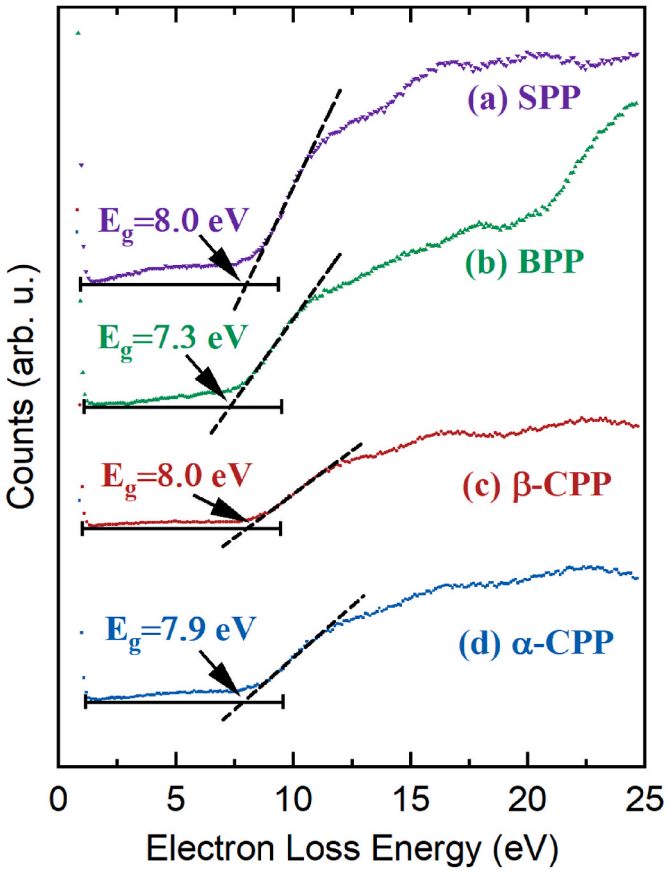

Fig. 4. REELS spectra of undoped **(a)** SPP, **(b)** BPP, **(c)** β-CPP, **(d)** α-CPP samples and the estimation of the bandgap values E_g.

Ba) sites of the respective compound; (2) broad spectral envelopes centred at around 350 mT, which suggest clustering effects of Gd^{3+} at higher dopant concentrations. The saturation of EPR signal intensities at relatively low Gd^{3+} concentrations indicates a relatively low solubility limit of the dopant ions in pyrophosphate samples, which is probably caused by the ionic size mismatch and charge disparity between the trivalent Gd^{3+} ion and the native divalent cations of the lattice. Thus, the obtained EPR results indicate a correlation with the possible formation of Gd-rich phases for higher doping content inferred from the XRD data (Fig. 1).

EPR spectra structure contains valuable information about the local environment of Gd^{3+} ions in the pyrophosphate samples. When Gd^{3+} ions are incorporated into a crystal lattice, the degenerate $^8S_{7/2}$ ground state undergoes zero-field splitting (ZFS), even in the absence of an external magnetic field. ZFS is sensitive to the local site symmetry and gives rise to distinct EPR signals, which can be quantitatively described using the spin Hamiltonian (SH) formalism:

$$\widehat{H} = g\mu_B B\widehat{S} + \widehat{S}\widetilde{D}\widehat{S}, \quad (1)$$

where g is the g-factor; μ_B – the Bohr magneton; B – external magnetic field; $\widehat{S}$ – electronic spin operator; $\widetilde{D}$ – ZFS tensor, which can be expressed by axial $D = 3D_z/2$ and rhombic $E = (D_x - D_y)/2$ ZFS parameters [30,31]. Eq. (1) is a simplified SH form, and higher-order operators should also be included to calculate the ZFS of an $S = 7/2$ system; however, such a detailed analysis is beyond the scope of this study.

Fig. 3 presents multifrequency EPR spectra simulations obtained with $g = 1.991 \pm 0.001$, $D = 924 \pm 50$ MHz, and $E = 234 \pm 50$ MHz for the β-CPP: 0.5 % Gd sample. The satisfactory agreement between the simulated and experimental spectra recorded at two microwave frequencies using this single parameter set indicates preferential incorporation of Gd^{3+} ions into a single crystallographic site of β-CPP. Such a result could not be replicated for α-CPP and SPP (the experimental data are presented in Fig. S1 of the supporting information file). For these hosts, a unique set of SH parameters could not be obtained due to the high spectral complexity arising from strongly overlapping signals, likely associated with multiple Gd^{3+} centres. Under such conditions, reliable simulations of powder EPR spectra become highly challenging. The EPR spectra of BPP: Gd^{3+} contrast with those of the other materials by pronounced broadening effects. This points to structural disorder and site-to-site variations in the local environment of Gd^{3+} ions. This observation is consistent with the reported disorder effects involving the bridging oxygen atoms in BPP [26].

REELS spectra of the investigated pyrophosphates are shown in Fig. 4. The bandgap values were estimated by linearly extrapolating the leading edge of inelastic energy loss to the baseline of the elastic peak, and the values were found to be 8.0, 7.3, 8.0, and 7.9 eV for undoped SPP, BPP, β-CPP, and α-CPP, respectively. Acquired results are similar to literature values for α-CPP and β-CPP [11,32], however, appear somewhat higher than reported SPP bandgap values obtained from optical measurements and DFT calculations (5.1 eV) [33]. This discrepancy may partly reflect differences between REELS-derived estimates and bulk bandgap estimation methods [34], including the surface sensitive nature of REELS and uncertainties associated with determining the energy-loss onset by linear extrapolation. Nevertheless, all obtained values remain substantially higher than the energy of the Gd^{3+} $^6P_{7/2} \rightarrow {}^8S_{7/2}$ radiative transition (~3.97 eV) and therefore do not affect the main conclusions regarding host suitability for UV-B emission.

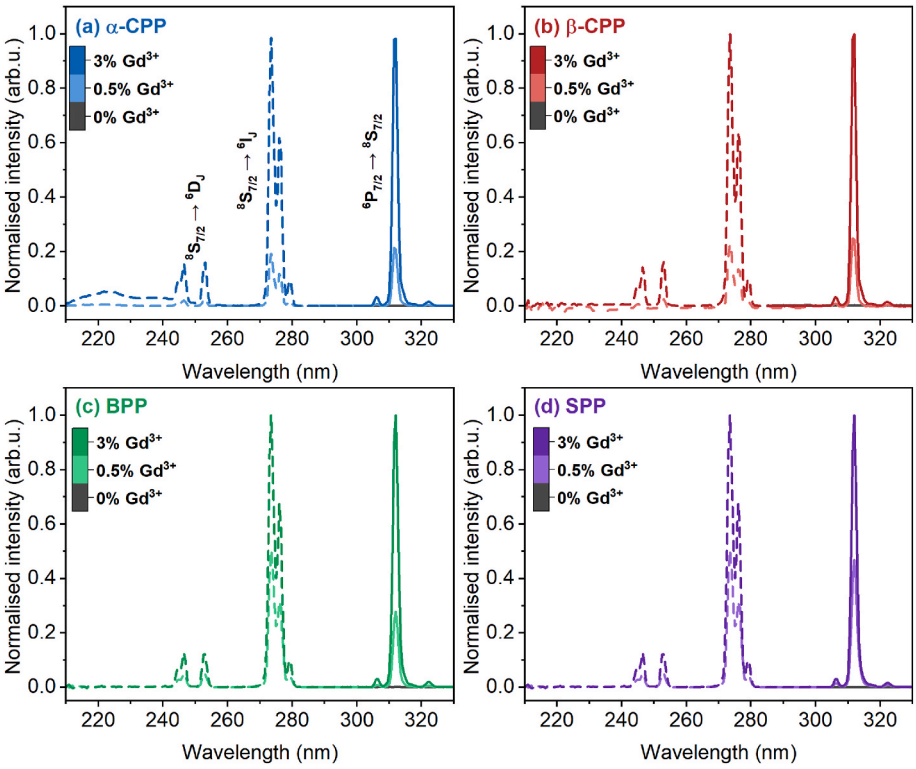

Fig. 5. Normalised room-temperature photoluminescence (solid lines) and excitation spectra (dashed lines) of **(a)** α-CPP, **(b)** β-CPP, **(c)** BPP, and **(d)** SPP samples.

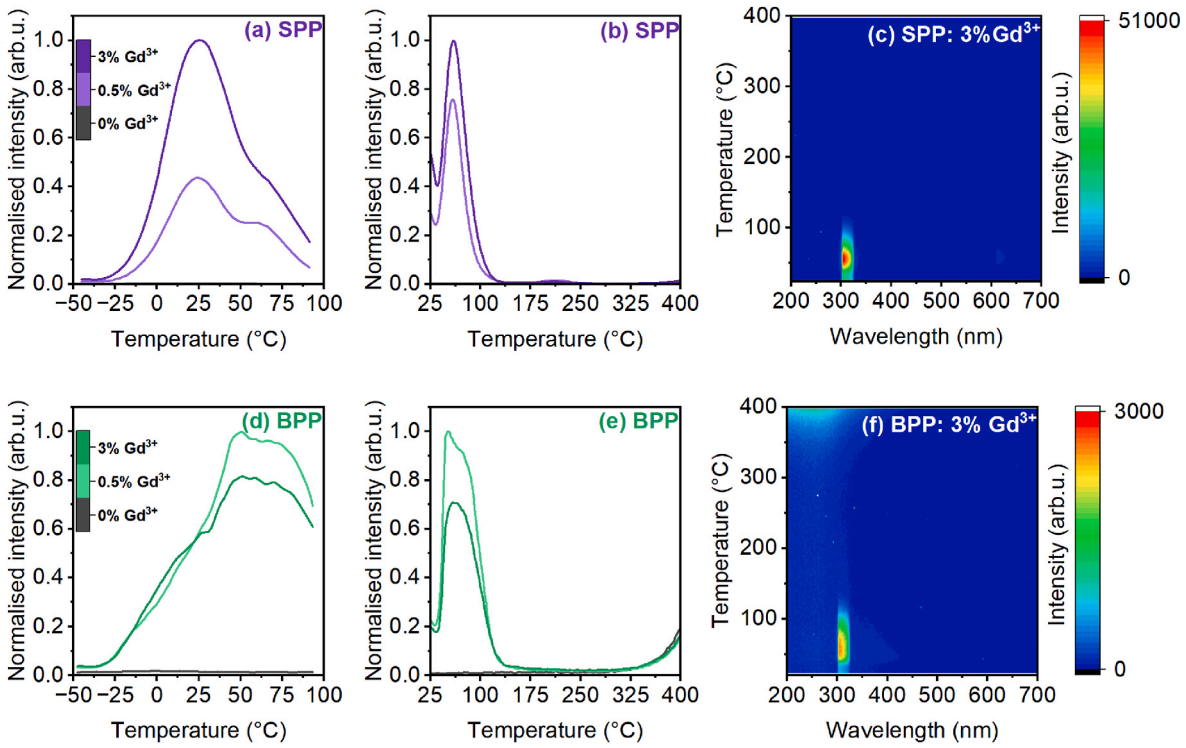

Fig. 6. TSL glow curves of SPP and BPP doped with Gd^{3+} in the **(a,d)** -50–100 °C range, **(b,e)** 25–400 °C range, **(c,f)** wavelength-resolved TSL contour plots.

3.2. Optical characterisation

The photoluminescence excitation and emission spectra of the investigated Gd-activated pyrophosphates are depicted in Fig. 5. Gd^{3+} ions exhibit a stable [Xe]$4f^7$ electron configuration that is known for its largely crystal-field-insensitive UV-B narrowband emission. Upon 273 nm excitation ($^8S_{7/2} \rightarrow {}^6I_J$), intensive $^6P_{7/2} \rightarrow {}^8S_{7/2}$ narrowband emission at 312 nm can be detected. Nearby shoulder bands around 306 nm and 322 nm can be attributed to the $^6P_{5/2} \rightarrow {}^8S_{7/2}$ transition and likely the phonon sideband of $^6P_{7/2} \rightarrow {}^8S_{7/2}$ radiative transition, respectively

Table 1
Estimated bandgap values and dominant trap depths of Gd^{3+}-activated pyrophosphates.

Material	Estimated bandgap of undoped host, E_g (eV)	Activation energy of the dominant traps (eV)
α-$Ca_2P_2O_7$: 3 % Gd^{3+}	7.9	≈0.6
β-$Ca_2P_2O_7$: 3 % Gd^{3+}	8.0	≈0.4
$Ba_2P_2O_7$: 3 % Gd^{3+}	7.3	≈0.6
$Sr_2P_2O_7$: 3 % Gd^{3+}	8.0	≈0.6, ≈0.7

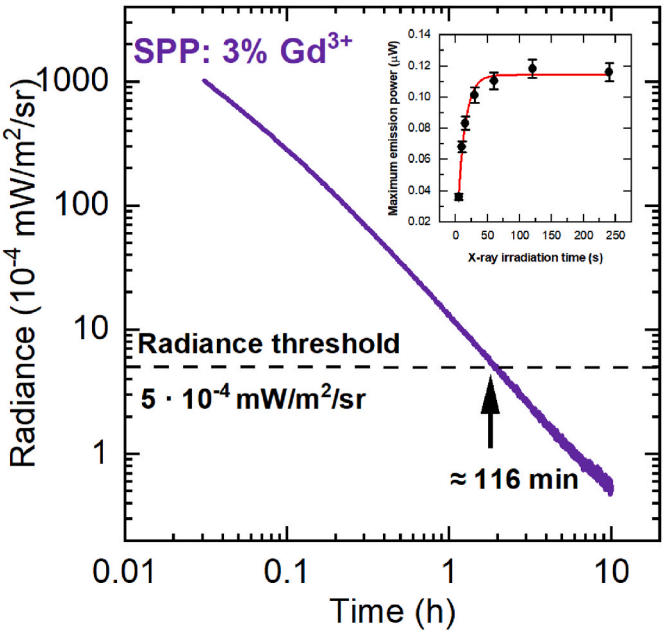

Fig. 7. Persistent luminescence kinetics after 3 min X-ray irradiation; inset: maximum persistent luminescence emission power as a function of irradiation time.

[35–37]. Excitation spectra (dashed lines in Fig. 5) were acquired by monitoring the 312 nm emission band. The excitation spectra consist of several narrow bands centred at 275 nm, 253 nm, and 246 nm, which are attributable to $^8S_{7/2} \rightarrow {}^6I_J$ and $^8S_{7/2} \rightarrow {}^6D_J$ transitions. For comparison of relative photoluminescence intensities between hosts, concentration-dependent integrated emission intensities are provided in the Supporting Information (Fig. S2).

TSL spectroscopy was used to characterise charge trapping processes induced by X-ray irradiation of the pyrophosphate samples. TSL glow curves were acquired in two different temperature ranges: (1) -50–100 °C to characterise shallow traps relevant to persistent luminescence and (2) 25–400 °C to investigate the deep traps. All TSL measurements (see Fig. 6 and Fig. S3) reveal Gd^{3+} emission with different TSL glow-peak temperatures for each host. Traps relevant to persistent luminescence typically exhibit TSL peaks in the range between 80 °C and 150 °C [38–40]. The best performance is observed for SPP and BPP samples (Fig. 6 (c) and (f)), where, during trap depopulation, Gd^{3+} acts as the only luminescence centre, and the intensity of the $^6P_{7/2} \rightarrow {}^8S_{7/2}$ transition centred at 312 nm is substantially higher than in both CPP polymorphs (Fig S3 (c) and (f)). The lower temperature TSL curves of SPP (Fig. 6 (a)) consist of two wide bands centred at around 25 °C and 65 °C. The 25 °C band potentially only plays a role in the initial emission, while the dominant contribution to persistent luminescence arises from the 65 °C band. A weak band at *ca.* 210 °C is also observed (Fig. 6 (b)); however, its contribution to persistent luminescence is likely minor. The TSL glow curves of BPP (Fig. 6(d) and (e)) suggest the presence of two closely overlapping bands that merge into a single wide feature peaking at 50 °C, covering the optimal temperature range for persistent luminescence. Similar to SPP, the emission is confined to the $^6P_{7/2} \rightarrow {}^8S_{7/2}$ transition of Gd^{3+} ions, although its intensity is comparatively lower (Fig. 6 (f)). To provide a semi-quantitative comparison of trapping characteristics relevant to persistent luminescence, approximate trap depths were estimated from the dominant TSL glow-peak temperatures using the empirical relation $E_a \approx T_m/500$ [41,42]. Owing to the broad and partially overlapping nature of the TSL glow curves, particularly in SPP and BPP, these values should be regarded as approximate and intended primarily for comparative discussion. The estimated values are summarised in Table 1.

Quantitative analysis of persistent luminescence metrics is based on emission power measurements. A benchmark luminance value of 0.32 mcd/m^2 is commonly used to assess the luminescence duration of persistent phosphors emitting in the visible range, considering the sensitivity of human eyes. For UV- and IR-emitting persistent phosphors, a radiometric threshold value of $5 \cdot 10^{-4}$ $mW/m^2/sr$ is generally accepted, which approximately equals the above-mentioned luminance value (at 555 nm, photopic vision) [8,43]. Persistent luminescence power density measurements (W/m^2) are therefore essential to evaluate the luminescence duration above the defined radiance threshold.

Radiance derived from persistent luminescence decay kinetics is shown in Fig. 7. Persistent luminescence measurements were performed on the 3 mol% Gd^{3+} samples, as this concentration exhibited the highest persistent luminescence intensity among the investigated compositions. Using a power-density evaluation methodology similar to that proposed by *Wang* et al. [44], for SPP: 3 % Gd^{3+}, we obtain power density estimations of 9.3 mW/m^2 and 6.1 mW/m^2 at 5 s and 10 s, respectively. Maximum emission power plateaus after ≈60 s of X-ray excitation, after which the available trapping sites are saturated and no further gain in intensity is observed (see the inset of Fig. 7). The luminescence signal in a laboratory setting can be detected for over 10 h, with its intensity above the radiance threshold persisting for ≈116 min. Due to the smaller initial TSL intensity (Fig. 6 (f)), the duration of persistent luminescence above the threshold of BPP: 3 % Gd^{3+} is shorter, lasting for approximately 45 min (Fig. S4).

3.3. Electron paramagnetic resonance (EPR)

EPR spectroscopy was employed to investigate radiation-induced radicals in the pyrophosphate samples, and the results are summarised in Fig. 8. X-ray irradiation generates distinct EPR signals in each host matrix, whereas the influence of Gd^{3+} doping on the formed defect types is comparatively minor. Namely, the dopant affects signal intensities - reflecting the concentration of paramagnetic centres - but does not shift resonance positions or introduce additional signals. This demonstrates that the same types of centres are formed irrespective of Gd^{3+} doping. Quantitative analysis of the double-integrated EPR signal intensities of X-ray-induced radicals as a function of Gd^{3+} concentration is presented in Fig. S5. A more detailed analysis of each host matrix is presented below.

The EPR spectra of β-CPP can be interpreted as a superposition of multiple signals with varying degrees of stability. Fig. S6 shows the assignment of the EPR spectrum to radicals labelled as β-1, β-2, and β-3 according to Ref. [14]. The least stable radical, β-1, can be assigned to an oxygen-related hole centre based on the principal values of the g-factor ($g_1 = 2.027$, $g_2 = 2.017$, $g_3 = 2.009$). The more stable centres exhibit highly overlapping signals, the precise origin of which remains uncertain.

EPR spectra simulations of the X-ray-induced radicals in all hosts were performed using the SH:

$$\hat{H} = g\mu_B B\hat{S} + \hat{S}A\hat{I}, \quad (2)$$

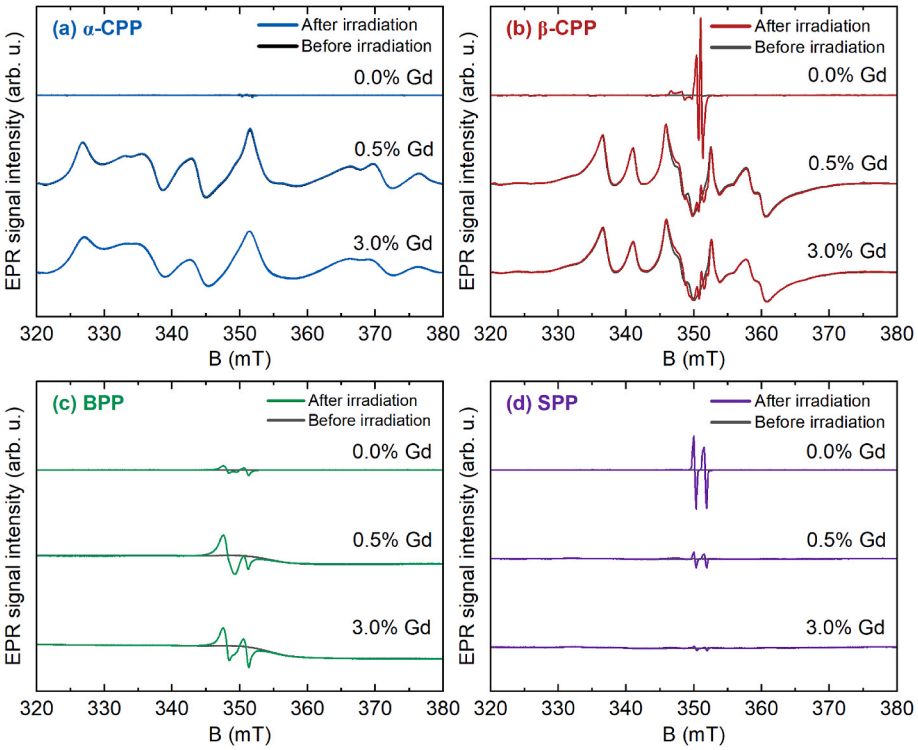

Fig. 8. EPR spectra (1 mW; 0.1 mT) of **(a)** α-CPP, **(b)** β-CPP, **(c)** BPP, and **(d)** SPP samples before and after irradiation with X-rays. EPR signal intensities are normalised to 100 mg of sample mass.

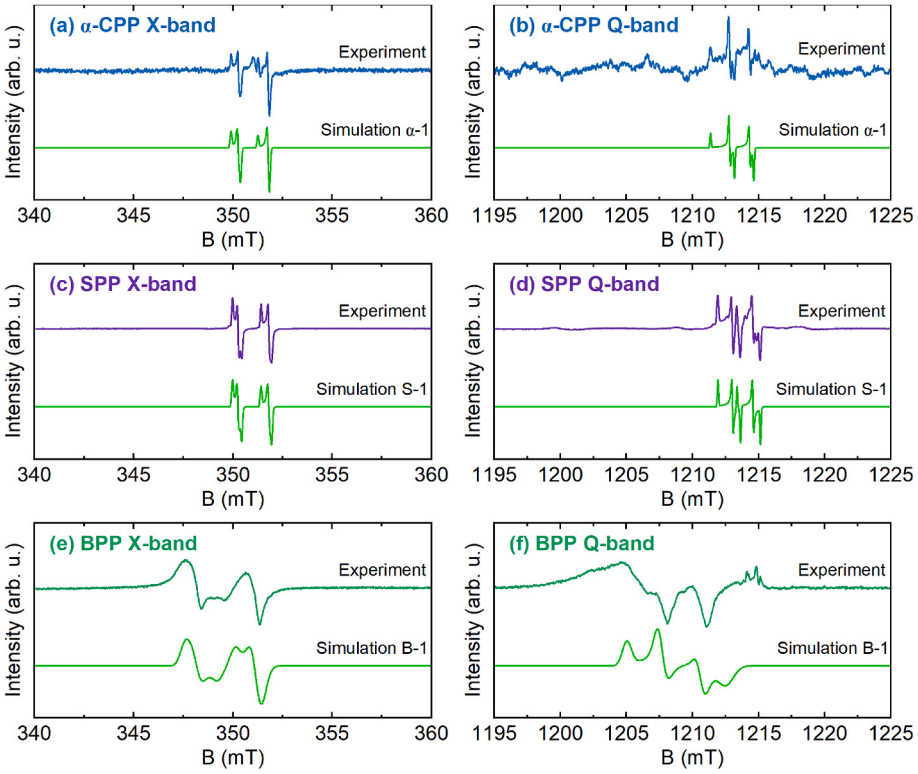

Fig. 9. Multifrequency EPR spectra simulations of X-ray-induced radicals in undoped **(a,b)** α-CPP, **(c,d)** SPP, and **(e,f)** BPP samples.

where A – hyperfine (HF) interaction tensor; $\hat{I}$ – nuclear spin operator. The radicals were modelled as electronic spin $S = 1/2$ systems, including HF interaction with a single ^{31}P nuclear spin ($I = 1/2$; 100 % natural abundance) where necessary. The simulations of room-temperature detected radicals are displayed in Fig. 9, while those additionally resolved in low-temperature EPR measurements are shown in Fig. S7–S9. Table 2 provides a summary of fitted SH parameters.

Table 2
SH parameters of X-ray-induced radicals in pyrophosphate samples.

Host	Radical	*g* factor			HF coupling with ^{31}P		
		g_1	g_2	g_3	A_1, MHz	A_2, MHz	A_3, MHz
α-CPP	α-1	2.0045	2.0020	2.0014	38	42	41
	α-2	2.0462	2.0103	2.0027			
SPP	S-1	2.0037	2.0018	2.0008	40	43	42
	S-2	2.0600	2.0133	2.0008			
	S-3	2.0190	2.0135	2.0120			
BPP	B-1	2.0144	2.0096	2.0057	71	83	62

Two distinct radiation-induced radicals are observed in α-CPP, consistent with previous reports [14]. The first centre, denoted α-1 (Fig. 9(a) and (b)), has a slightly anisotropic g-factor with the average value close to the free-electron value of $g_e = 2.0023$. The unpaired spin exhibits nearly isotropic HF interaction with a single ^{31}P nucleus. The hyperfine coupling is smaller than that typically reported for PO_4- and PO_3- type radicals in solids [45], indicating a relatively low spin density on the phosphorus atom. The second radical, α-2, could be resolved in low-temperature EPR measurements (Fig. S7). The highly anisotropic g-factor, combined with the absence of discernible hyperfine structure, suggests that it is an oxygen-centred trapped-hole O^- radical [45].

Optimisation of EPR detection temperature and microwave power (Fig. 9 (c), (d), Fig S8) allows for the detection of at least three radicals in SPP. S-1 and S-2 appear to be analogous to α-1 and α-2, but with slightly different SH parameters due to variations in the local structure of the trapping sites. Radical S-3 has a positive shift relative to the g_e value and a relatively small anisotropy, which suggests that the radical is probably delocalized on oxygen.

The dominant contribution to the EPR spectra following X-ray irradiation in BPP arises from a single radical assigned as B-1. The considerable ^{31}P hyperfine coupling, together with the positive g-shift, indicates substantial spin density on phosphorus in comparison to other hosts. However, EPR spectra variations with Gd^{3+} concentration (Fig. 8 (c)) and microwave power (Fig. S9) reveal the presence of an additional signal overlapping the low-field component of this doublet.

Fig. 10 shows the stability of X-ray–induced radicals determined through stepwise annealing experiments. Clear differences are observed in the annealing kinetics of the phosphorus-related radical α-1 and the O^--type radical α-2 in α-CPP (Fig. 10 (d)). Radical α-1 is relatively stable and is likely associated with the deeper traps responsible for the TSL glow peak at *ca.* 250 °C (Fig S3 (b)), whereas radical α-2 anneals within the temperature range of the low-temperature glow peak near 100 °C. In SPP, radical annealing proceeds in multiple stages (Fig. 10 (e)). In the first stage (150–250 °C), the low-temperature radicals S-2 and S-3 are completely annealed, accompanied by a partial reduction of the S-1 EPR signal intensity. A second stage of S-1 annealing occurs between 400 and 600 °C. However, none of these processes show a clear correlation with the TSL curve of SPP (Fig. 6 (b)), which implies that the detected EPR-active radicals are not directly involved in recombination luminescence processes in SPP. In BPP, the phosphorus-related radical B-1 exhibits relatively low stability (Fig. 10 (f)), consistent with the low-temperature TSL glow peaks observed in the 20-110 °C range (Fig. 6 (e)). The correlation between the annealing kinetics of B-1 and low-temperature TSL signals suggests that phosphorus-related hole traps may contribute to persistent luminescence in BPP.

4. Discussion

The results demonstrate that alkaline earth pyrophosphates are promising host lattices for Gd^{3+} doping, enabling luminescence in the

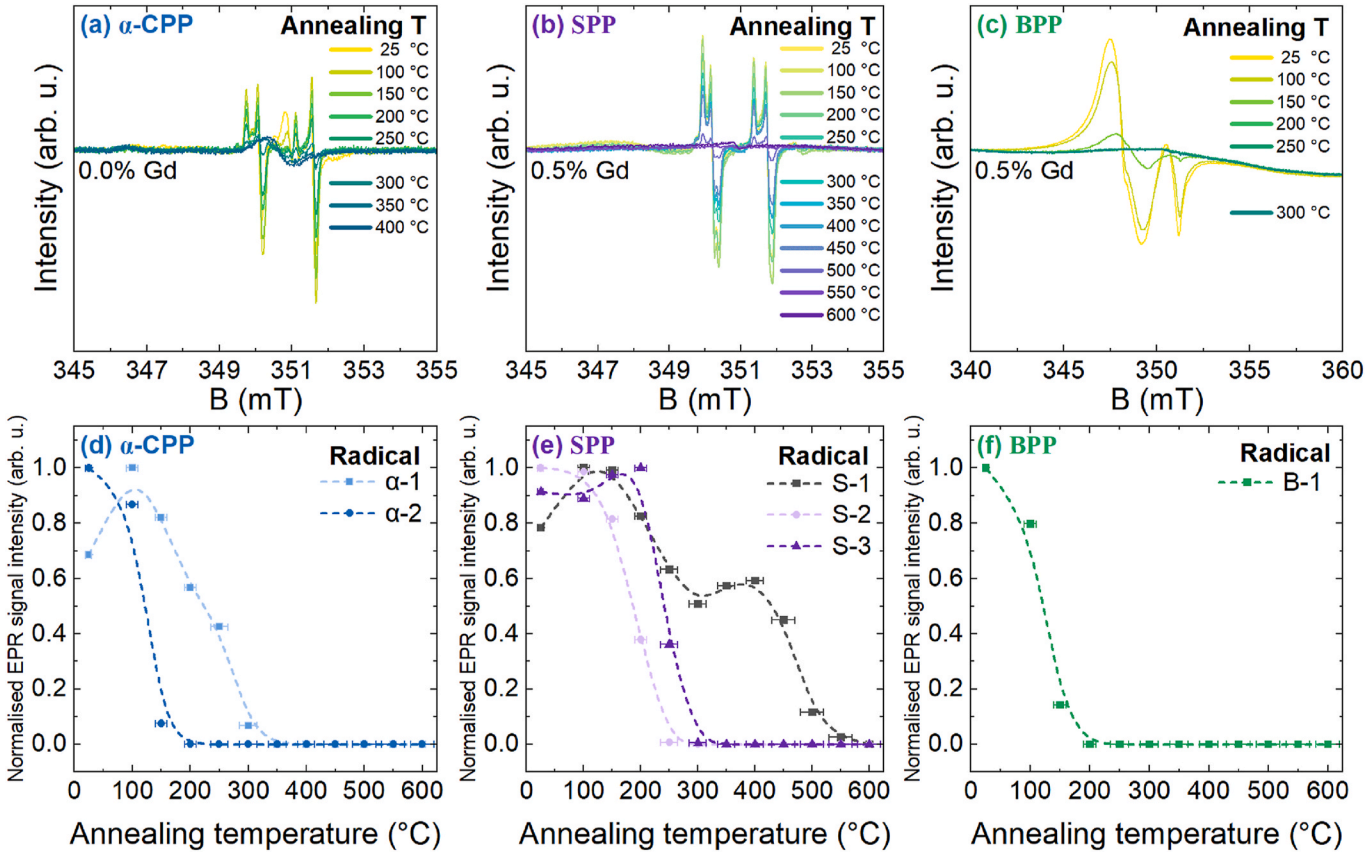

Fig. 10. EPR spectra (1 mW; 0.1 mT) acquired after sample annealing at selected temperatures and the corresponding annealing kinetics of **(a,d)** α-CPP, **(b,e)** SPP, and **(c,f)** BPP. The low-temperature-detected EPR spectra are shown in **Figs.EPR.S7-S9**.

Table 3
Comparison of persistent luminescence parameters reported for representative UV-emitting phosphors.

Material	Excitation	Emission λ (nm)	Power density (mW/m^2)	Duration above threshold (h)	Duration above detector background (h)	Ref.
$Ca_2Al_2SiO_7$: Ce^{3+}	350 nm	410	12.55 (10 s)	48	>48	[48]
$Ca_2Al_2SiO_7$: Pr^{3+}	250 nm	268	10.6 (10 s)	3.7	>16	[21]
	X-rays	268	7.4 (10 s)	10.5	>16	[21]
		268	4.8 (10 s)			[44]
$LiYGeO_4$: Bi^{3+}	254 nm	365	11.83 (10 s)		>72	[49]
$Sr_2P_2O_7$: Gd^{3+}	X-rays	312	15.2 (1 s)	≈2	>10	This work
			9.3 (5 s)			
			5.8 (10 s)			
	X-rays	312	12.57 (20 s)			[18]
$Ba_2P_2O_7$: Gd^{3+}	X-rays	312	1.5 (1 s)	≈0.75	>10	This work
			0.8 (5 s)			
			0.6 (10 s)			

UV spectral range. The determined bandgap values vary in the 7-8 eV range (Fig. 4), exceeding the energy of the Gd^{3+} $P_{7/2} \rightarrow {}^8S_{7/2}$ transition at 312 nm (3.97 eV) (Fig. 5). At high dopant levels, however, XRD (Fig. 1) and EPR (Fig. 2) analyses indicate limited solubility of Gd^{3+}, leading to clustering and the formation of secondary crystalline phases. These findings reveal the importance of considering charge compensation mechanisms in the pyrophosphate matrices and suggest that co-doping may be necessary to further optimise luminescence performance. A reasonable strategy is co-doping with monovalent alkali metal ions such as Li^+, Na^+, or K^+, which could provide charge compensation for substitution of divalent alkaline earth cations by trivalent rare-earth ions [46,47]. Since the investigated pyrophosphates differ in crystal structure and local alkaline-earth coordination, differences in Gd^{3+} incorporation and defect formation are expected. This is reflected in the distinct Gd^{3+} incorporation environments observed by EPR spectroscopy for α-CPP, β-CPP, SPP and BPP. Moreover, local structural variations also influence the formation and stability of radiation-induced defect centres. During X-ray excitation, the pyrophosphate materials undergo charge-transfer processes that generate paramagnetic species (Fig. 8) and, in some cases, efficient persistent luminescence (Fig. 7). The induced radicals can be categorised into trapped-hole centres and phosphorous-related radicals, exhibiting distinct thermal stabilities (Fig. 10). The thermal stimulation of some of the trapping centres occurs gradually at room temperature, which enables long-lasting luminescence emission (Fig. 6). A comparison of persistent luminescence parameters of representative UV-emitting phosphors is provided in Table 3. Among the investigated pyrophosphate hosts, the highest UV persistent luminescence radiance is observed for SPP: 3 % Gd^{3+} (Fig. 7). The obtained performance is comparable to previously reported UV-emitting phosphors. Some of the X-ray-induced radicals in the pyrophosphate materials are highly stable, storing the excitation energy in deep traps. Therefore, defect-engineering strategies increasing the concentration of shallow traps should be pursued to achieve the full potential of these materials. In addition, for application-oriented use, further investigation of photostability under prolonged irradiation and thermal quenching behaviour at elevated temperatures will be important to assess operational stability under realistic conditions. Overall, these results highlight the dual role of alkaline earth pyrophosphates as efficient hosts for both UV photoluminescence and persistent luminescence, positioning them as promising candidates for advanced UV-B phosphor applications.

5. Conclusions

Gd^{3+}-doped alkaline-earth pyrophosphates ($Ca_2P_2O_7$, $Sr_2P_2O_7$, and $Ba_2P_2O_7$) were comparatively investigated to evaluate how host composition influences Gd^{3+} incorporation, defect formation, and UV-B persistent luminescence. Structural analyses confirmed successful Gd^{3+} incorporation at low-to-moderate concentrations, while $GdPO_4$ impurity formation at higher Gd^{3+} concentrations indicated limited solubility in selected hosts. EPR spectroscopy revealed host-dependent incorporation of Gd^{3+}: single-site substitution in β-$Ca_2P_2O_7$, multisite formation in α-$Ca_2P_2O_7$ and $Sr_2P_2O_7$, and pronounced structural disorder effects in the case of $Ba_2P_2O_7$.

X-ray irradiation generated oxygen-related hole centres and phosphorus-related radicals with different thermal stabilities, with the annealing kinetics partially correlated with TSL glow curves, indicating the involvement of these defect states in luminescence processes in some hosts. Among the investigated materials, $Sr_2P_2O_7$: 3 % Gd^{3+} exhibited the most favourable persistent luminescence at room temperature, maintaining emission above the accepted radiance threshold for nearly 2 h. Overall, the results demonstrate that alkaline-earth pyrophosphates are promising UV-B phosphor hosts, while also highlighting the importance of defect and charge-compensation engineering strategies for further optimisation of energy storage and release processes.

CRediT authorship contribution statement

Didzis Salnajs: Writing – review & editing, Writing – original draft, Visualization, Methodology, Investigation, Formal analysis, Conceptualization. **Dace Nilova:** Writing – original draft, Methodology, Investigation. **Jonas Stadulis:** Writing – review & editing, Investigation. **Anatolijs Sarakovskis:** Writing – review & editing, Investigation. **Aleksej Zarkov:** Writing – review & editing, Investigation. **Andris Antuzevics:** Writing – review & editing, Writing – original draft, Supervision, Investigation, Conceptualization.

Declaration of generative AI and AI-assisted technologies in the manuscript preparation process

During the preparation of this work the author(s) used ChatGPT to improve sentence structure and language. After using this tool, the author(s) reviewed and edited the content as needed and take(s) full responsibility for the content of the published article.

Declaration of competing interest

The authors declare that they have no known competing financial interests or personal relationships that could have appeared to influence the work reported in this paper.

Acknowledgements

This research is funded by the Latvian Council of Science, post-doctoral research project No. 1.1.1.9/LZP/1/24/013 “Ultraviolet persistent luminescence in biocompatible phosphates: defect studies in novel materials”.

D. Salnajs gratefully acknowledges the financial support from the European Regional Development Fund and Latvian state budget grant in the framework for the project “Strengthening the doctoral research and development capacity of the University of Latvia in smart specialization areas” No 1.1.1.8/1/24/I/003.

Appendix A. Supplementary data

Supplementary data to this article can be found online at https://doi.org/10.1016/j.matchemphys.2026.132800.

Data availability

Data will be made available on request.

References

[1] A.A. Sharma, M. Rakshita, P.P. Pradhan, K.A.K. Durga Prasad, S. Mishra, K. Jayanthi, D. Haranath, Efficacy of photodynamic therapy using UVB radiation-emitting novel phosphor material for non-surgical treatment of psoriasis, J. Mater. Res. 38 (2023) 2812–2822, https://doi.org/10.1557/s43578-023-01008-7.

[2] X. Wang, Y. Chen, P.A. Kner, Z. Pan, Gd^{3+} -activated narrowband ultraviolet-B persistent luminescence through persistent energy transfer, Dalton Trans 50 (2021) 3499–3505, https://doi.org/10.1039/D1DT00120E.

[3] X. Zhou, J. Qiao, Y. Zhao, K. Han, Z. Xia, Multi-responsive deep-ultraviolet emission in praseodymium-doped phosphors for microbial sterilization, Sci. China Mater. 65 (2022) 1103–1111, https://doi.org/10.1007/s40843-021-1790-1.

[4] L. Liu, H. Guo, L. Wang, Q. Shi, J. Qiao, C. Cui, P. Huang, Ultraviolet-A persistent luminescence and photocatalytic application of $Y_3Ga_3MgSiO_{12}$:Bi^{3+} phosphor, J. Alloys Compd. 1009 (2024) 176852, https://doi.org/10.1016/j.jallcom.2024.176852.

[5] Y. Mei, H. Xu, J. Zhang, Z. Ci, M. Duan, S. Peng, Z. Zhang, W. Tian, Y. Lu, Y. Wang, Design and spectral control of a novel ultraviolet emitting long lasting phosphor for assisting TiO_2 photocatalysis: Zn_2SiO_4:Ga^{3+}, Bi^{3+}, J. Alloys Compd. 622 (2015) 908–912, https://doi.org/10.1016/j.jallcom.2014.11.003.

[6] S. Lai, Z. Yang, J. Liao, J. Qiu, Z. Song, Y. Yang, D. Zhou, Investigation of persistent luminescence property of Bi^{3+}, Dy^{3+} co-doped $CdSiO_3$ phosphor, Mater. Res. Bull. 60 (2014) 714–718, https://doi.org/10.1016/j.materresbull.2014.09.049.

[7] W. Yuan, T. Tan, H. Wu, R. Pang, S. Zhang, L. Jiang, D. Li, Z. Wu, C. Li, H. Zhang, Intense UV long persistent luminescence benefiting from the coexistence of Pr^{3+}/Pr^{4+} in a praseodymium-doped $BaLu_2Al_2Ga_2SiO_{12}$ phosphor, J. Mater. Chem. C 9 (2021) 5206–5216, https://doi.org/10.1039/D1TC00584G.

[8] D. Poelman, D. Van Der Heggen, J. Du, E. Cosaert, P.F. Smet, Persistent phosphors for the future: fit for the right application, J. Appl. Phys. 128 (2020), https://doi.org/10.1063/5.0032972.

[9] V. Singh, B.R. Venkateswara Rao, A.S. Rao, J.L. Rao, M. Irfan, Photoluminescence and electron spin resonance study on narrow-band UVB emitting Gd-doped $LaPO_4$ phosphors, Optik 206 (2020) 164020, https://doi.org/10.1016/j.ijleo.2019.164020.

[10] D. Griesiute, E. Garskaite, A. Antuzevics, V. Klimavicius, V. Balevicius, A. Zarkov, A. Katelnikovas, D. Sandberg, A. Kareiva, Synthesis, structural and luminescent properties of Mn-doped calcium pyrophosphate ($Ca_2P_2O_7$) polymorphs, Sci. Rep. 12 (2022), https://doi.org/10.1038/s41598-022-11337-y.

[11] T. Pier, F. Schröder, J. Kappelhoff, J. Hopster, T. Jüstel, On the photoluminescence of Pr(III) activated $Ca_2P_2O_7$ polymorphs, J. Lumin. 277 (2025), https://doi.org/10.1016/j.jlumin.2024.120934.

[12] W. He, Y. Xie, Q. Xing, P. Ni, Y. Han, H. Dai, Sol-gel synthesis of biocompatible Eu^{3+}/Gd^{3+} co-doped calcium phosphate nanocrystals for cell bioimaging, J. Lumin. 192 (2017) 902–909, https://doi.org/10.1016/j.jlumin.2017.08.033.

[13] M.R. Squillante, T. Jüstel, R.R. Anderson, C. Brecher, D. Chartier, J.F. Christian, N. Cicchetti, S. Espinoza, D.R. McAdams, M. Müller, B. Tornifoglio, Y. Wang, M. Purschke, Fabrication and characterization of UV-emitting nanoparticles as novel radiation sensitizers targeting hypoxic tumor cells, Opt. Mater. 80 (2018) 197–202, https://doi.org/10.1016/j.optmat.2018.04.033.

[14] A. Antuzevics, J. Cirulis, G. Krieke, D. Griesiute, A. Beganskiene, A. Kareiva, A. Dubauskas, V. Klimavicius, A. Zarkov, Paramagnetic radiation-induced radicals in calcium pyrophosphate polymorphs, Mater. Chem. Phys. 310 (2023), https://doi.org/10.1016/j.matchemphys.2023.128479.

[15] S. Xu, S. sha Liu, C. Zhao, T. Han, D. Zhu, Luminescent properties of single-phase $Ba_2P_2O_7$:Tb^{3+}, R (R = Eu^{2+}, Ce^{3+}) phosphors for white LED, J, Mater. Sci.: Mater. Electron. 28 (2017) 10061–10066, https://doi.org/10.1007/s10854-017-6766-0.

[16] L. Li, M. Peng, B. Viana, J. Wang, B. Lei, Y. Liu, Q. Zhang, J. Qiu, Unusual concentration induced antithermal quenching of the Bi^{2+} emission from $Sr_2P_2O_7$:Bi^{2+}, Inorg. Chem. 54 (2015) 6028–6034, https://doi.org/10.1021/acs.inorgchem.5b00887.

[17] H. Li, Y. Yang, P. Li, D. Peng, L. Li, Force-induced ultraviolet C luminescence of Pr_3 $_+$-Doped $Sr_2P_2O_7$ for X-Ray dosimetry, Adv. Mater. (2024), https://doi.org/10.1002/adma.202411804.

[18] Y. Zhang, Y. Liang, X. Shan, D. Chen, S. Miao, R. Shi, F. Xie, W. Wang, X-ray-Excited long-lasting narrowband Ultraviolet-B persistent luminescence from Gd_{3+}-Doped $Sr_2P_2O_7$ phosphor, Inorg. Chem. 61 (2022) 20647–20656, https://doi.org/10.1021/acs.inorgchem.2c03584.

[19] M.H.V. Werts, Making sense of Lanthanide Luminescence, Sci. Prog. 88 (2005) 101–131, https://doi.org/10.3184/003685005783238435.

[20] S. Stoll, A. Schweiger, EasySpin, a comprehensive software package for spectral simulation and analysis in EPR, J. Magn. Reson. 178 (2006) 42–55, https://doi.org/10.1016/j.jmr.2005.08.013.

[21] A. Antuzevics, G. Krieke, G. Doke, P. Rodionovs, D. Nilova, J. Cirulis, A. Fedotovs, U. Rogulis, Role of paramagnetic aluminum hole centers in UV-C persistent luminescence of $Ca_2Al_2SiO_7$:Pr^{3+}, J. Phys. Chem. C (2024) https://doi.org/10.1021/acs.jpcc.4c06848.

[22] D. Griesiute, E. Raudonyte-Svirbutaviciene, A. Kareiva, A. Zarkov, The influence of annealing conditions on the Ca/P ratio and phase transformations in bulk calcium phosphates, CrystEngComm 24 (2022) 1166–1170, https://doi.org/10.1039/D1CE01625C.

[23] J.-J. Bian, D.-W. Kim, K.-S. Hong, Phase transformation and sintering behavior of $Ca_2P_2O_7$, Mater. Lett. 58 (2004) 347–351, https://doi.org/10.1016/S0167-577X(03)00498-1.

[24] C. Calvo, Crystal structure of .alpha.-calcium pyrophosphate, Inorg. Chem. 7 (1968) 1345–1351, https://doi.org/10.1021/ic50065a019.

[25] L.-O. Hagman, I. Jansson, C. Magnéli, O. Tolboe, J. Paasivirta, The crystal structure of alpha-$Sr_2P_2O_7$, Acta Chem. Scand. 22 (1968) 1419–1429, https://doi.org/10.3891/acta.chem.scand.22-1419.

[26] A.A. ElBelghitti, A. Elmarzouki, A. Boukhari, E.M. Holt, σ-Dibarium pyrophosphate, Acta Crystallogr. C 51 (1995) 1478–1480, https://doi.org/10.1107/S0108270195001739.

[27] Y.Q. Jia, Crystal radii and effective ionic radii of the rare earth ions, J. Solid State Chem. 95 (1991) 184–187, https://doi.org/10.1016/0022-4596(91)90388-X.

[28] R.D. Shannon, Revised effective ionic radii and systematic studies of interatomic distances in halides and chalcogenides, Acta Crystallogr., Sect. A 32 (1976) 751–767, https://doi.org/10.1107/S0567739476001551.

[29] J. Hölsä, T. Laamanen, M. Lastusaari, P. Novák, Defect aggregates in the $Sr_2MgSi_2O_7$ persistent luminescence material, J. Rare Earths 29 (2011) 1130–1136, https://doi.org/10.1016/S1002-0721(10)60611-4.

[30] J. Telser, EPR interactions - zero-field splittings, in: R.K. Harris, R.L. Wasylishen (Eds.), Emagres, John Wiley & Sons, Ltd, Chichester, UK, 2017, pp. 207–234, https://doi.org/10.1002/9780470034590.emrstm1501.

[31] J.A. Weil, Electron Paramagnetic Resonance: Elementary Theory and Practical Applications, second ed., Wiley-Interscience, Hoboken, N.J, 2007.

[32] T.N. Nurakhmetov, T.T. Alibay, K.B. Zhangylyssov, A.S. Nurpeissov, S. Pazylbek, D. Griesiute, A. Zarkov, A. Kareiva, Luminescence and Electron–Hole-Trapping centers in α-$Ca_2P_2O_7$−Mn, Crystals 14 (2024) 406, https://doi.org/10.3390/cryst14050406.

[33] Y. Zhong, M. Xia, Z. Chen, P. Gao, H.T. (Bert) Hintzen, W.-Y. Wong, J. Wang, Z. Zhou, Pyrophosphate phosphor solid solution with high quantum efficiency and thermal stability for efficient LED lighting, iScience 23 (2020) 100892, https://doi.org/10.1016/j.isci.2020.100892.

[34] M. Vos, S.W. King, B.L. French, Measurement of the band gap by reflection electron energy loss spectroscopy, J. Electron. Spectrosc. Relat. Phenom. 212 (2016) 74–80, https://doi.org/10.1016/j.elspec.2016.08.001.

[35] F. Moretti, N. Chiodini, M. Fasoli, L. Griguta, A. Vedda, Optical absorption and emission properties of Gd^{3+} in silica host, J. Lumin. 126 (2007) 759–763, https://doi.org/10.1016/j.jlumin.2006.11.009.

[36] U. Vetter, J. Zenneck, H. Hofsäss, Intense ultraviolet cathodoluminescence at 318 nm from Gd^{3+}-doped AlN, Appl. Phys. Lett. 83 (2003) 2145–2147, https://doi.org/10.1063/1.1605237.

[37] X. Shan, X. Lv, D. Chen, Y. Zhang, L. Huang, Y. Liang, Synergistic integration of NB-UVB persistent luminescence and concentration-dependent photochromism in a phosphate phosphor for multifunctional applications, Adv. Opt. Mater. 13 (2025) e01335, https://doi.org/10.1002/adom.202501335.

[38] J. Hassinen, J. Hölsä, T. Laamanen, M. Lastusaari, P. Novák, Electronic structure of defects in $Sr_2MgSi_2O_7$:Eu^{2+}, La^{3+} persistent luminescence material, J. Non-Cryst. Solids 356 (2010) 2015–2019, https://doi.org/10.1016/j.jnoncrysol.2010.06.035.

[39] A. Jain, A. Kumar, S.J. Dhoble, D.R. Peshwe, Persistent luminescence: an insight, Renew. Sustain. Energy Rev. 65 (2016) 135–153, https://doi.org/10.1016/j.rser.2016.06.081.

[40] Q. Liu, Z.-Y. Feng, H. Li, Q. Zhao, N. Shirahata, Y. Kuroiwa, C. Moriyoshi, C.-K. Duan, H.-T. Sun, Non-rare-earth UVC persistent phosphors enabled by bismuth doping, Adv. Opt. Mater. 9 (2021) 2002065, https://doi.org/10.1002/adom.202002065.

[41] K. Van Den Eeckhout, P.F. Smet, D. Poelman, Persistent luminescence in Eu^{2+}-Doped compounds: a review, Materials 3 (2010) 2536–2566, https://doi.org/10.3390/ma3042536.

[42] Cambridge Solid State Science Series) S. W. S. Mckeever - Thermoluminescence of Solids, Cambridge University Press, 1988 (2), (n.d.).

[43] J. Xu, S. Tanabe, Persistent luminescence instead of phosphorescence: history, mechanism, and perspective, J. Lumin. 205 (2019) 581–620, https://doi.org/10.1016/j.jlumin.2018.09.047.

[44] X. Wang, Y. Chen, F. Liu, Z. Pan, Solar-blind ultraviolet-C persistent luminescence phosphors, Nat. Commun. 11 (2020), https://doi.org/10.1038/s41467-020-16015-z.

[45] A.S. Marfunin, Spectroscopy, Luminescence and Radiation Centers in Minerals,(n.d.).

[46] Y. Xiang, L. Zhong, Y. Long, S. Liu, Z. Cheng, S. Rao, J. Hong, B. Lei, H. Suo, J. Zhang, L. Zhou, F. Wang, M. Wu, Deciphering defect-mediated anti-thermal quenching multimodal luminescence for information encryption, Adv. Mater. 38 (2026) e15825, https://doi.org/10.1002/adma.202515825.

[47] R. Steinbach, A. Ohlsen, T. Pier, T. Jüstel, On the Pr^{3+} activated and Li^{+} co-doped α-$Sr_2P_2O_7$ for high-energy excitation, J. Lumin. 293 (2026) 121840, https://doi.org/10.1016/j.jlumin.2026.121840.

[48] D. Nilova, D. Salnajs, G. Doke, A. Antuzevics, Excitation-dependent ultraviolet-visible persistent luminescence and charge trapping in $Ca_2Al_2SiO_7$: Ce^{3+}, Opt. Mater. 174 (2026) 117969 https://doi.org/10.1016/j.optmat.2026.117969.

[49] J. Shi, X. Sun, S. Zheng, X. Fu, Y. Yang, J. Wang, H. Zhang, Super-long persistent luminescence in the ultraviolet A region from a Bi^{3+} -doped $LiYGeO_4$ phosphor, Adv. Opt. Mater. 7 (2019) 1900526, https://doi.org/10.1002/adom.201900526.